

# Weierstraß-Institut für Angewandte Analysis und Stochastik Leibniz-Institut im Forschungsverbund Berlin e. V.

Preprint

ISSN 0946 – 8633

## Computational haemodynamics in stenotic internal jugular veins

Alfonso Caiazzo<sup>1</sup>, Gino Montecinos<sup>2</sup>, Lucas O. Müller<sup>2</sup>,

E. Mark Haacke<sup>3</sup>, Eleuterio F. Toro<sup>2</sup>

submitted: June 3, 2013

<sup>1</sup> Weierstrass Institute  
Mohrenstr. 39  
10117 Berlin  
Germany  
E-Mail: [Alfonso.Caiazzo@wias-berlin.de](mailto:Alfonso.Caiazzo@wias-berlin.de)

<sup>2</sup> Laboratory of Applied Mathematics, DICAM  
University of Trento  
Via Mesiano 77, Povo, Italy  
E-Mail: [gino.montecinos@ing.unitn.it](mailto:gino.montecinos@ing.unitn.it)  
[lucas.mueller@ing.unitn.it](mailto:lucas.mueller@ing.unitn.it)  
[toro@ing.unitn.it](mailto:toro@ing.unitn.it)

<sup>3</sup> MR Research Facility  
Wayne State University  
Detroit, USA  
E-Mail: [nmrimaging@aol.com](mailto:nmrimaging@aol.com)

No. 1793  
Berlin 2013



---

2010 *Physics and Astronomy Classification Scheme*. 07.05.Tp, 47.11.-j, 47.63.Cb, 87.19.uj.

*Key words and phrases*. Computational haemodynamics, stenosis, internal jugular veins, anomalous haemodynamics, CCSVI.

Edited by  
Weierstraß-Institut für Angewandte Analysis und Stochastik (WIAS)  
Leibniz-Institut im Forschungsverbund Berlin e. V.  
Mohrenstraße 39  
10117 Berlin  
Germany

Fax: +49 30 20372-303  
E-Mail: [preprint@wias-berlin.de](mailto:preprint@wias-berlin.de)  
World Wide Web: <http://www.wias-berlin.de/>

## Abstract

Stenosis in internal jugular veins (IJVs) are frequently associated to pathological venous circulation and insufficient cerebral blood drainage. In this work, we set up a computational framework to assess the relevance of IJV stenoses through numerical simulation, combining medical imaging, patient-specific data and a mathematical model for venous occlusions. Coupling a three-dimensional (3D) description of blood flow in IJVs with a reduced one-dimensional model (1D) for major intracranial veins, we are able to model different anatomical configurations, an aspect of importance to understand the impact of IJV stenosis in intracranial venous haemodynamics. We investigate several stenotic configurations in a physiologic patient-specific regime, quantifying the effect of the stenosis in terms of venous pressure increase and wall shear stress patterns. Simulation results are in qualitative agreement with reported pressure anomalies in pathological cases. Moreover, they demonstrate the potential of the proposed multiscale framework for individual-based studies and computer-aided diagnosis.

## 1 Introduction

Internal jugular veins (IJVs) are the main paths of discharge of blood from brain towards the heart for most subjects in supine position. When these paths are perturbed, cerebral venous drainage is assured by collateral circles. The potential higher pressures and consequences on cerebral blood flow still need to be fully understood. Chronic CerebroSpinal Venous Insufficiency (CCSVI) is a recently described vascular condition [41, 42] which is characterized by an anomalous cerebral venous drainage. Such discovery has given rise to the still controversial hypothesis that such venous pathology can be correlated to Multiple Sclerosis [43, 41]. IJV stenoses, defined as occlusions of the blood vessel, represent one of the diagnosis criteria of CCSVI. In this context, stenoses, as other venous anomalies, are assessed *non-invasively* through MRI and Echo-Colour Doppler imaging, which allows visualisation of the morphology of cerebral veins and the main characteristics of blood flow. These criteria, however, are strongly dependent on subjective evaluation and often do not take into account specific anatomical features of patients. In particular, stenoses are mainly diagnosed based on the reduction in the cross-sectional area (e.g. below to  $0 \leq 0.3 \text{ cm}^2$  [41]).

In recent years, computational haemodynamics has become a valuable, non-invasive alternative tool for gaining additional insight on patient haemodynamics, in terms of flow patterns, pressure, wall shear stress (see, e.g., [16, 19, 36, 40]), as well as for computing clinically relevant indicators [14, 17]. When patient-specific geometries are available from medical imaging, these computational methods are based on the numerical solution of the three-dimensional (3D) incompressible Navier-Stokes equations (on compliant or fixed structure), to describe the blood flow, tuned according to the available measurements. However, the feasibility of detailed computer simulation is still limited by the prohibitive computational cost, especially when considering a large number of blood vessels and complex topologies. This issue is particularly

important when modelling the haemodynamics of veins, as small vessels and minor collaterals (which are usually neglected in arterial blood flow modelling) might be determinant for the physiological flow conditions. In order to reduce the model complexity, 3D models are often used in combination with reduced one-dimensional (1D) models, to simulate haemodynamics in large vessel networks (see *e.g.* [4, 10, 11, 20, 26]), and *lumped parameter* or zero-dimensional (0D) models, which are introduced to take into account the influence of smaller and terminal vessels (see, *e.g.*, [38, 39]). A further application of these reduced models is the simulation of one-dimensional stenoses, modelled as a reduction of vessel cross sectional area [29, 24].

In this paper we propose a multiscale computational framework to support the diagnosis and the characterization of internal jugular vein stenoses. To this end we will first construct a model of IJV stenosis in a realistic context, by deforming locally a patient-specific geometry, obtained from medical imaging. Through a geometrical multiscale model, taking into account realistic flow rates profiles for the straight sinuses and brachiocephalic veins, we investigate different scenarios involving *occlusions of the IJVs of different severity* and *different morphologies of cerebral veins*. Computationally, stenoses will be characterised through the perturbation of cerebral haemodynamics as function of the reduction of cross sectional area of the jugular veins. Haemodynamics quantities to monitor include pressure increase across the stenosis (a criteria used for diagnosis in *e.g.* [37, 41]), peak velocity increase [18] and wall shear stress. As a result, our study provides the possibility of improving these diagnosis criteria, through a detailed investigation of flow field perturbation and considering variable veins morphology.

The rest of the paper is organized as follows. In Section 2 we describe the tools and the algorithms used for the setup of our *in-silico* stenotic vein model, while the methodologies for the numerical simulations of stenotic jugular veins is described in Section 3. Section 4 describes the setup of the computational study, while results are presented in Section 5 and discussed in detail in Section 6. Finally, conclusions are drawn in Section 7.

## 2 Anatomical model set up

### 2.1 Data acquisition

Patients data and medical images used in this study have been obtained from the Detroit MR Imaging Center (Wayne State University, Detroit, MI, USA). Data were obtained following the MRI protocols described in [37], specifically designed to assess CCSVI, with particular focus on the imaging of head, neck, and spine (to image the azygos system). The veins of interest for the present study were imaged using *2D time-of-flight MR venography* and *3D contrast-enhanced MR angiography/venography*. Imaged vessels include the superior vena cava, brachiocephalic veins, internal jugular veins and dural sinuses. These vessels are responsible for almost the totality of cerebral venous drainage towards the heart in supine position. Besides anatomical images, 2D phase-contrast MRI (PC-MRI) flow acquisitions have been collected in the neck, positioned according to the cervical vertebrae at the C2/ C3 level. Manually defined contours on PC-MRI allowed for quantification of flow variables, including average velocity, positive (toward the brain), negative (toward the heart), and combined volume flow rates [37].

## 2.2 Image segmentation

MRI data has been segmented using the open-source software VMTK (*Vascular Modeling ToolKit*, [1, 32]). In particular, we extracted the surface representation of the two IJVs, right and left brachiocephalic veins, up to the superior vena cava and the subclavian veins (Figure 1, left). From the triangulated surface geometries, three-dimensional meshes for computational analysis were obtained using the open-source mesh generator TetGen [30].

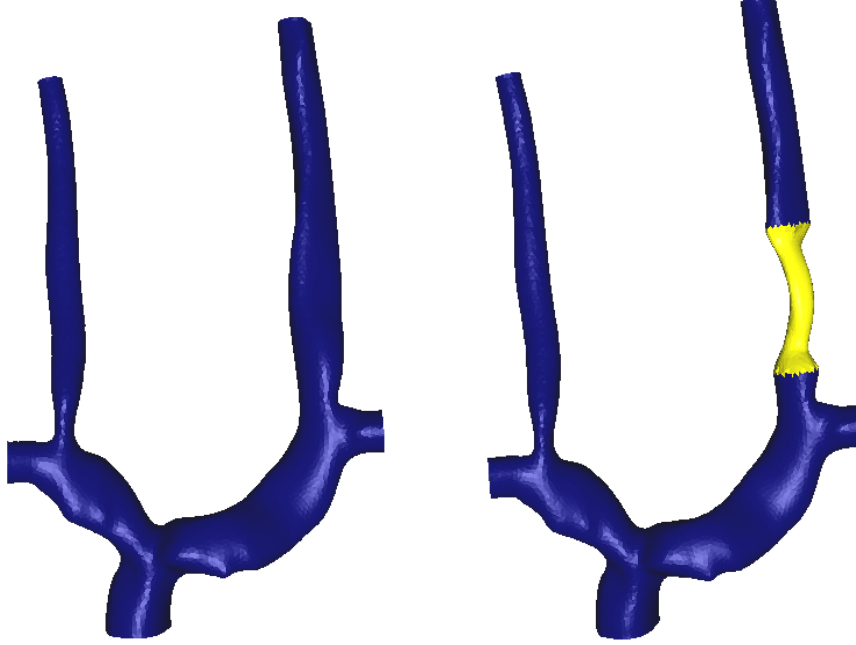


Figure 1: **Left:** View of a patient surface geometry after segmentation. **Right:** Stenotic geometry, with a local CSA reduction of 77% along the left IJV (in yellow).

## 2.3 Mathematical model of a stenosis

Our goal is to set up a model for blood flow in stenotic veins, able to take into account realistic flow conditions as well as the realistic patients anatomies. To this end we adopted a computational procedure to create *stenotic IJVs* artificially, starting from the geometry of a healthy (i.e. non stenotic) patient. Let us denote with  $\mathcal{S}$  a given patient surface geometry (see Figure 1, left), and with  $\Omega$  the corresponding three-dimensional computational domain. In order to obtain a stenotic geometry, we consider the computational domain  $\Omega$  as it would be filled with an ideal elastic material at rest. The narrowing of cross sectional area, defining the stenosis, is then created applying an external compression force on a small subset  $\Gamma_{\text{sten}}$  of the surface  $\mathcal{S}$ . In practice, the new computational domain is obtained solving a partial differential equation for a displacement field  $\mathbf{d} : \Omega \rightarrow \mathbb{R}^3$ :

$$\begin{aligned}
 \nabla \cdot \boldsymbol{\sigma}_e(\mathbf{d}) &= 0, \text{ on } \Omega \\
 \mathbf{d} &= 0, \text{ on } \partial\Omega/\Gamma_{\text{sten}} \\
 \boldsymbol{\sigma}_e(\mathbf{d})\mathbf{n} &= -\mathbf{f}_{\mathbf{n}}, \text{ on } \Gamma_{\text{sten}},
 \end{aligned} \tag{1}$$

where  $\sigma_e(\mathbf{d})$  plays the role of the second Piola-Kirchhoff stress tensor for an elastic material, related to the  $\nabla \mathbf{d}$  through a constitutive law, *e.g.*

$$\sigma_e(\mathbf{d}) = \kappa (\nabla \mathbf{d} + \nabla \mathbf{d}^T), \quad \kappa > 0$$

(for a linear elastic model). In (1),  $\mathbf{f}_n$  is a normal force, whose entity (to be tuned according to the particular geometry) defines the reduction of the cross sectional area. From the solution of (1), the deformed surface is recovered by adding the displacement  $\mathbf{d}$  to the original geometry. Figure 1 (right) shows a particular result of this procedure.

### 3 Computational haemodynamics

#### 3.1 Three-dimensional blood flow modelling

In order to simulate the blood flow in internal jugular veins, we consider the boundary of the computational domain  $\Omega$  partitioned as

$$\partial\Omega = \Gamma_{\text{in}} \cup \Gamma_{\text{wall}} \cup \Gamma_{\text{out}},$$

denoting, respectively, the *inflow* boundaries, the *vessel wall* and the *outflow* boundaries.

The images have been acquired in supine position, when the internal jugular veins represent the main discharge path for cerebral blood flow, and have relatively low volume changes during the cardiac cycle. Hence, as a first approximation, we consider the domain  $\Omega$  to be constant in time. Considering the blood as an incompressible, Newtonian fluid, an approximation of blood flow on  $\Omega$  is obtained solving the incompressible Navier-Stokes equations for the velocity  $\mathbf{u} : \Omega \times \mathbb{R}^+ \rightarrow \mathbb{R}^3$  and the pressure  $p : \Omega \times \mathbb{R}^+ \rightarrow \mathbb{R}$

$$\left\{ \begin{array}{ll} \rho \partial_t \mathbf{u} + \rho \mathbf{u} \cdot \nabla \mathbf{u} + \nabla p - 2\mu \operatorname{div} \varepsilon(\mathbf{u}) = 0 & \text{in } \Omega, \\ \operatorname{div} \mathbf{u} = 0 & \text{in } \Omega, \\ \mathbf{u} = \mathbf{u}_{\text{in}} & \text{on } \Gamma_{\text{in}}, \\ \mathbf{u} = 0 & \text{on } \Gamma_{\text{wall}}, \\ \sigma(\mathbf{u}, p) \mathbf{n} = p_{\text{out}} & \text{on } \Gamma_{\text{out}}. \end{array} \right. \quad (2)$$

In (2)  $\rho$  stands for the density of the fluid (1060 Kg/m<sup>3</sup>) and the fluid Cauchy-stress tensor is given by

$$\sigma(\mathbf{u}, p) = -p\mathbf{I} + 2\mu\varepsilon(\mathbf{u}), \quad \varepsilon(\mathbf{u}) \stackrel{\text{def}}{=} \frac{1}{2} (\nabla \mathbf{u} + \nabla \mathbf{u}^T),$$

$\mu$  being the dynamic viscosity of the fluid ( $4 \cdot 10^{-3}$  Pa · s).

Moreover,  $\mathbf{u}_{\text{in}}$  and  $p_{\text{out}}$  represent a given inlet velocity and a given outlet pressure, imposed at inflow and outflow boundaries, respectively. In order to simulate a physiologic regime, these values have been prescribed based on realistic flow rate and pressure profiles (see Section 4.1).

##### 3.1.1 Numerical solution

In order to numerically solve problem (2), we consider first a time-discretization based on a Chorin-Temam projection scheme [5, 13, 31]. In this approach, velocity and pressure are

computed separately in two sub-steps. Let  $t_n$  denote the time at the  $n$ -th time step performed with an uniform time step  $\tau$ . For a given initial condition  $\mathbf{u}^0 = \mathbf{u}_0$ , each time step consists of solving the following two problems:

$$\left\{ \begin{array}{l} \rho \frac{\mathbf{u}^{n+1} - \mathbf{u}^n}{\tau} + \rho \mathbf{u}^n \cdot \nabla \mathbf{u}^{n+1} - 2\mu \nabla \cdot \boldsymbol{\varepsilon}(\mathbf{u}^{n+1}) + \nabla p^n = 0 \quad \text{in } \widehat{\Omega}, \\ \mathbf{u}^n = \mathbf{u}_{\text{in}}(t_{n+1}) \quad \text{on } \Sigma_{\text{in}}, \\ 2\mu \boldsymbol{\varepsilon}(\mathbf{u}^{n+1}) \mathbf{n} = 0 \quad \text{on } \Sigma_{\text{out}}, \\ \mathbf{u}^n = 0 \quad \text{on } \Sigma_{\text{wall}}. \end{array} \right. \quad (3)$$

$$\left\{ \begin{array}{l} -\frac{\tau}{\rho} \Delta p^{n+1} = -\nabla \cdot \mathbf{u}^{n+1} \quad \text{in } \widehat{\Omega}, \\ \frac{\tau}{\rho} \frac{\partial p^{n+1}}{\partial \mathbf{n}} = 0 \quad \text{on } \Sigma_{\text{in}} \cup \Sigma_{\text{wall}}, \\ p^{n+1} = p_{\text{out}}^{n+1} \quad \text{on } \Sigma_{\text{out}}. \end{array} \right. \quad (4)$$

Problems (3)-(4) are solved using continuous piece-wise linear finite elements on the tetrahedral mesh. In this semi-discrete version, inlet flow rates are imposed through Dirichlet boundary conditions on the velocity field in equation (3), while the outlet pressure is imposed as a Dirichlet condition in (4), see [3].

### 3.2 One-dimensional blood-flow model

Due to their relatively high computational cost, full 3D fluid models can be currently used to resolve the blood flow only *locally*, i.e. focusing on a limited number of vessels. In order to investigate the cerebral haemodynamics from a more general point of view, one has to reduce the complexity of the original Navier-Stokes equations (2). This can be done considering the cardiovascular system as a network of interconnected and compliant vessels, in which the flow is assumed to be one-dimensional. Integrating the mass and momentum conservation equations (2) over each pipe cross section one obtains (see, *e.g.*, [28])

$$\left\{ \begin{array}{l} \frac{\partial A}{\partial t} + \frac{\partial}{\partial x} (uA) = 0, \\ \frac{\partial (uA)}{\partial t} + \frac{\partial}{\partial x} (\hat{\alpha} u^2 A) + \frac{A}{\rho} \frac{\partial p}{\partial x} = f, \end{array} \right. \quad (5)$$

where  $A(x, t)$  is the cross sectional area along the longitudinal axis,  $u(x, t)$  the cross-sectional averaged axial velocity,  $p(x, t)$  the average internal pressure over the cross-section,  $f(x, t)$  stands for the friction force per unit length, and the parameter  $\hat{\alpha}$  depends on the shape of the velocity profile along the cross section (usually assumed equal to 1, which corresponds to a constant velocity over the cross section). As in (2),  $\rho$  denotes the blood density.

System (5) for the three unknowns  $A$ ,  $u$  and  $p$  requires a closure condition. This is usually accomplished via a *tube law* involving a pressure-area relation. In this manner the vessel deformation is related to changes in transmural pressure [27], namely

$$p(x, t) = p_e(x, t) + K(x) \phi(A(x, t), A_0(x)), \quad (6)$$

with

$$\phi(A, A_0) = \left( \frac{A}{A_0} \right)^m - \left( \frac{A}{A_0} \right)^n. \quad (7)$$

Here  $p_e(x, t)$  denotes the external pressure,  $K(x)$  is the bending stiffness of the vessel wall (related the Young modulus, the wall thickness, and the vessel radius in an unloaded reference configuration), while  $A_0(x)$  denotes the cross-sectional area at reference pressure.

### 3.2.1 Numerical scheme for the 1D model

We reformulate (5) in quasilinear form as proposed in [34]:

$$\partial_t \mathbf{Q} + \mathbf{A}(\mathbf{Q}) \partial_x \mathbf{Q} = \mathbf{S}(\mathbf{Q}), \quad (8)$$

in terms of the unknowns

$$\mathbf{Q} = [A, q, K, A_0, p_e]^T, \quad (9)$$

where  $q = Au$  is the mass flow rate. Now the source term vector in (8) is

$$\mathbf{S}(\mathbf{Q}) = [0, -f, 0, 0, 0]^T \quad (10)$$

and the coefficient matrix  $\mathbf{A}(\mathbf{Q})$  is given by

$$\mathbf{A}(\mathbf{Q}) = \begin{bmatrix} 0 & 1 & 0 & 0 & 0 \\ c^2 - u^2 & 2u & \frac{A}{\rho} \phi & K \frac{A}{\rho} \frac{\partial \phi}{\partial A_0} & \frac{A}{\rho} \\ 0 & 0 & 0 & 0 & 0 \\ 0 & 0 & 0 & 0 & 0 \\ 0 & 0 & 0 & 0 & 0 \end{bmatrix}, \quad (11)$$

$c = \sqrt{\frac{A}{\rho} K \frac{\partial \phi}{\partial A}}$  being the wave speed. See [34] for the details of the derivation and for a detailed mathematical analysis of the system.

We solve numerically system (8) using a high-order ADER finite volume scheme [35], with the DET solver for the generalised Riemann problem [8]. As is well known, all GRP solvers require in addition a classical Riemann solver (piece-wise constant data), see [21]; to this end here we adopt the Dumber-Osher-Toro (DOT) scheme [9], with a modification described in [23]. For a full description of the global, closed-loop multi-scale model see [22]. For background on the ADER approach and recent developments see [33] (Chapters 19 and 20) and references therein.

### 3.3 Geometrical multiscale model

To take into account the effect of the upstream veins on the haemodynamics of stenotic IJVs, we consider a multi-scale model combining the local three-dimensional finite element solver for stenotic IJVs with a one-dimensional network containing the sigmoid sinuses, the transverse sinuses, the straight and the sagittal sinuses (see Figure 2).

From the computational point of view, the coupled model consists of solving equations (2) and equations (8) on two separate domains. The outgoing fluxes from the one-dimensional model, at each 3D-1D interface, are used to impose inlet boundary conditions for the velocity in (2), prescribing a 3D velocity profile satisfying

$$q_{3D}^{n+1} = q_{1D}^{n+1},$$



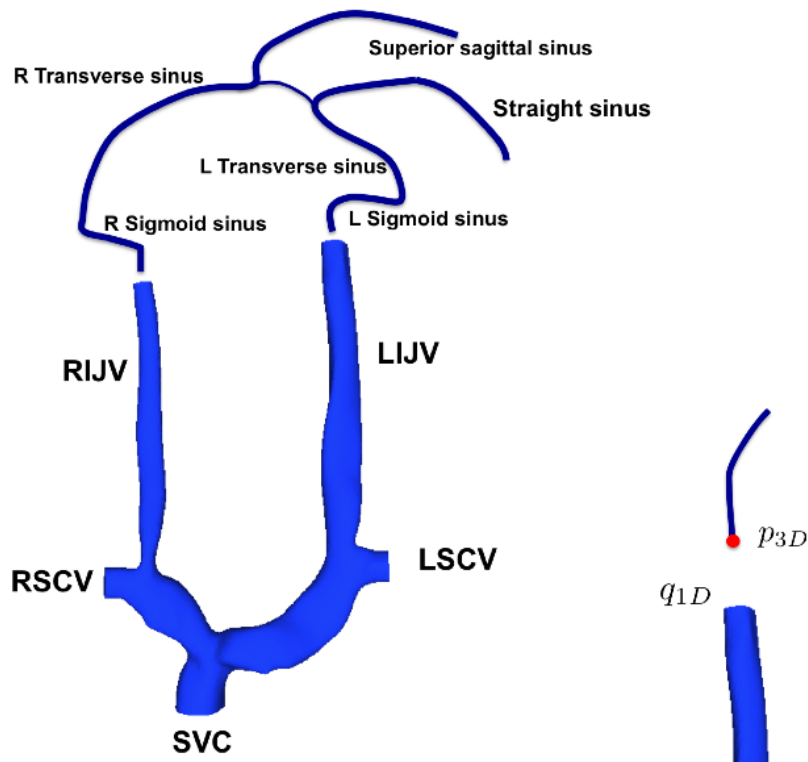


Figure 2: **Left:** Sketch of the multiscale 3D-1D model. Fluid 3D simulations are used for the jugular veins, up to the superior vena cava, while a 1D network represents intracranial veins up to the level of straight and superior sagittal sinuses. **Right:** The coupling is defined imposing the outgoing 1D flow to the 3D model (2), and imposing the resulting pressure as boundary condition for (8), at the ends of the 1D network.

while the resulting 3D pressures are used to modify the boundary conditions of problem (8) at the end of the network (Figure 2, right). The pressure coupling is implemented following the approach proposed in [26] (in the form of a preconditioned Richardson iteration), setting the 1D pressure as

$$p_{1D}^{n+1} = \gamma p_{3D}^{n+1} + (1 - \gamma) p_{1D}^n$$

for a parameter  $\gamma \in (0, 1]$ .

### 3.4 Computation of Wall Shear Stress

Besides the velocity and pressure fields, another quantity of clinical relevance is the Wall Shear Stress (WSS), defined as the tangential component of the normal shear stress at the vessel wall:

$$\tau_{\text{WSS}} \stackrel{\text{def}}{=} \tau_{\mathbf{n}} - (\tau_{\mathbf{n}} \cdot \mathbf{n}) \mathbf{n} \quad (12)$$

(where  $\tau_{\mathbf{n}} = \mathbf{n}^T \nabla \mathbf{u}$  denotes the normal shear stress).

In fact, it has been shown that an abnormal WSS might affect the biology of endothelial cells, playing a relevant role in the development of pathologies and in the triggering of inflammatory responses (see, *e.g.*, [2, 16, 25]).

In this context, an important mechanical indicator, monitoring the oscillatory behaviour in time of WSS, is the so-called Oscillatory Stress Index (OSI), defined as

$$\text{OSI}_{\text{WSS}} \stackrel{\text{def}}{=} \frac{1}{2} \left( 1 - \frac{\|\langle \tau_{\text{WSS}} \rangle\|}{\langle \|\tau_{\text{WSS}}\| \rangle} \right), \quad (13)$$

where  $\langle \cdot \rangle$  stands for the average value over a period (cardiac cycle). Namely, the OSI quantifies the WSS vector deflection from blood flow predominant direction (varying from 0.0, for no-cyclic variation of WSS vector, to 0.5, for 180 degrees deflection of WSS direction).

In computational haemodynamics, the calculation of accurate wall shear stresses is a relatively complex issue, as it strongly depends on the level of approximation of the surface geometry (hence on the quality of the medical images). Using piecewise linear finite elements for the three-dimensional fluid solutions (Section 3.1.1), the velocity on the surface is approximated by linear polynomials, which results in a piecewise constant distribution of gradients. In order to reconstruct a smoother stress distribution at the surface nodes, we have computed nodal approximations of the velocity gradient considering all the neighbouring mesh points using then the smoothing and approximation procedure recently described in [7].

## 4 Case studies

Starting from a patient-specific reference domain for a healthy subject (not diagnosed as having a stenosis), we consider different set-ups of the computational model, which are depicted in Figure 3. First, we create artificial stenosis of increasing severity, using the procedure described in Section 2.3, obtaining CSA reductions from 20% up to 77% at the bottom of the left IJV (Figure 3, bottom). At the same time, in order to take into account the effect of upstream veins, we coupled the computational 3D domain to a 1D network of compliant vessels up to

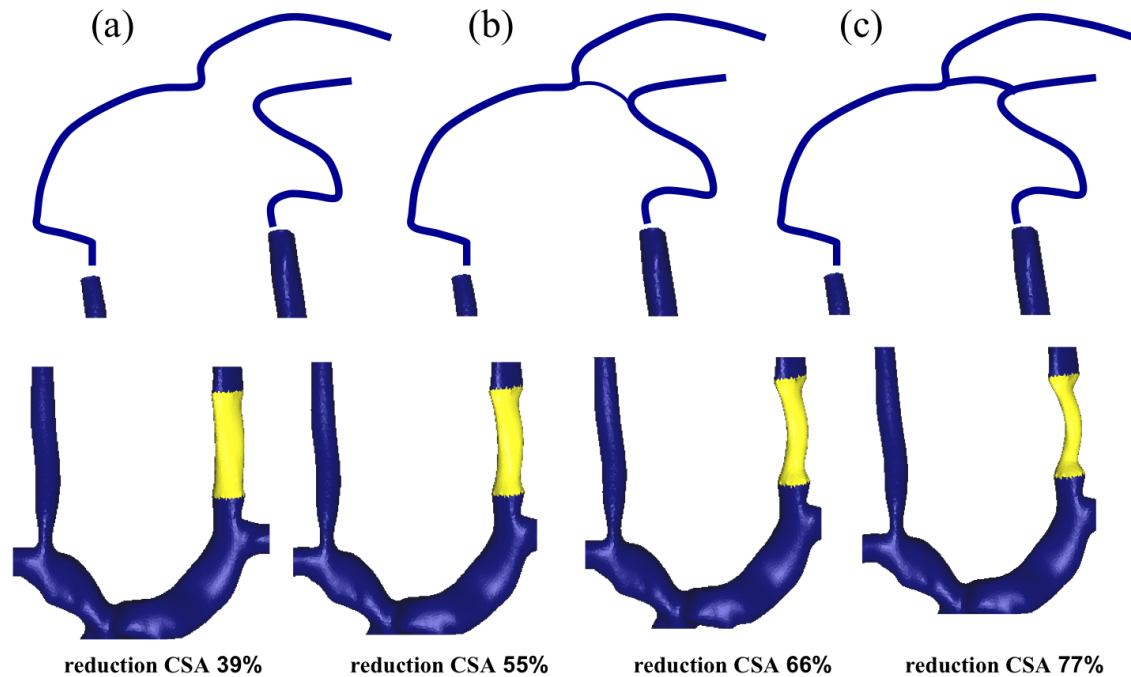


Figure 3: Model setups considered in our study. At the top, the different one-dimensional networks modelling the cerebral veins up to the straight and superior sagittal sinuses, considering the cases of disconnected, weakly connected and strongly connected sinuses (a, b and c, respectively). At the bottom, different stenotic geometries (with reduction of CSA of 39%, 55%, 66% and 77%, respectively) obtained perturbing the original patient-specific mesh at the bottom of the left IJV.

the Straight Sinus (STS) and Superior Sagittal Sinus (SSS), through the geometrical multi-scale method described in Section 3.3. Anatomical studies have shown that in about 50% of the population the SSS is drained by both transverse sinuses, whereas in the remaining cases drainage is unilateral [12]. This aspect might play a relevant role in the presence of a stenosis, as the connection between sinuses represents an important alternative discharge path in case of stenosis (as will be illustrated in Sections 5.2–5.3). Hence, in order to account for the variability of the intracranial venous network topology, three different versions of the multi-scale model have been considered:

- no connection between transverse sinuses (Figure 3a);
- weak connection (Figure 3b);
- strong connection (Figure 3c).

These different upstream models have been investigated in combination with all the different stenotic configurations.

## 4.1 Physiological boundary conditions

On each computational (3D-1D) domain, the blood flow has been simulated through the coupled approach described in Section 3. As boundary conditions, we prescribe values obtained from a closed-loop one-dimensional reduced model for the cardiovascular system [22]. We impose flow rates at the inlet boundaries for terminal ends of STS, SSS, Veins of Labbe (VLs) and Subclavian Veins (SCVs) and pressure at the SVC outlet (see Figure 4).

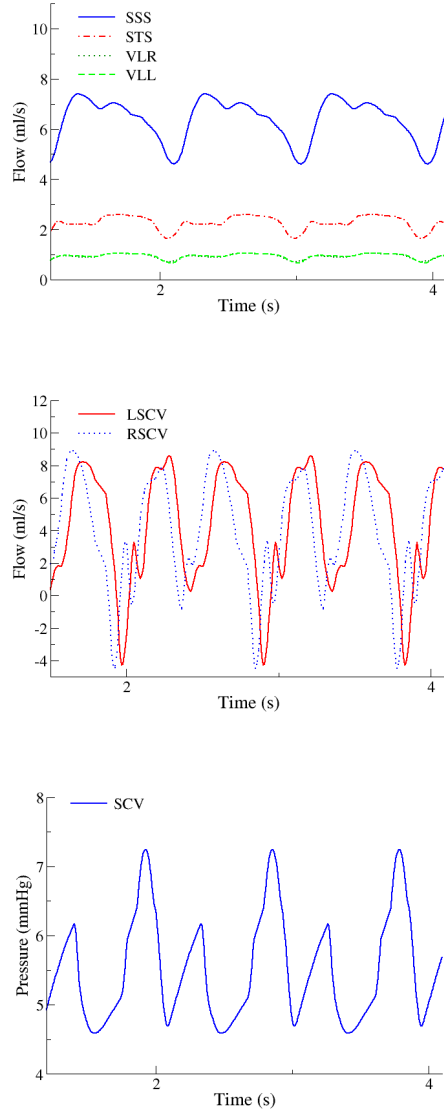


Figure 4: Flow rates and pressure used as boundary conditions for the 3D-1D computational model [22]. **Top:** Flow rates for the SSS, STS, left Vein of Labbe (VLL) and right Vein of Labbe (VLR). **Middle:** Flow rates for the left Subclavian Vein (LSCV) and right Subclavian Veins (RSCV). **Bottom:** Pressure profile imposed at the Superior Vena Cava (SVC).

## 5 Simulation results

This section presents the outcome of our computational study on the effect of a progressive IJV stenosis. In particular, we assessed the impact of an IJV stenosis according to

- the maximum pressure drop, defined as the pressure difference between IJV inlet and SVC outlet, as measured in [42],
- the peak velocity ratio, which refers to the ratio between the maximum pre-stenotic and post-stenotic velocities [18],
- the perturbation induced on the flow, in terms of WSS and OSI.

But first, in the following subsection, we partially validate our model by confronting simulated values against observations.

### 5.1 Comparison of numerical results against measured data

In Figure 5, we compare numerically computed flow rates at C2/C3 level for the *weak confluence* configuration (without stenosis) vs PC-MRI flow quantification data for the same patient. The qualitative and quantitative agreement for the left IJV is very satisfactory, both for the average flow (computed value of 6.68 ml/s versus a measured flow of 6.98 ml/s) and for the pulsatility. For the case of the right IJV we obtain similar average flow rates (compute flow rate of 2.94 ml/s versus a measured average flow of 4.18 ml/s), while flow rate and flow rate pulsatility are both lower than the ones obtained from PC-MRI measurements. This mismatch could be caused by several reasons. Amongst others, the fact that in the three-dimensional model we neglected minor collaterals, which might modify the time-dependent mass inflow.

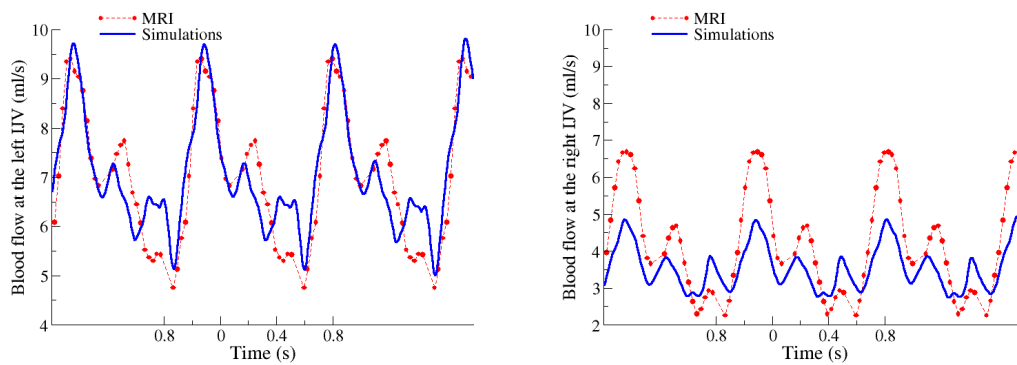


Figure 5: **Top:** Comparison of numerically computed flow rate (Simulation, full line) and PC-MRI measurements (MRI, dashed line) for the left IJV at C2/C3 level. **Bottom:** Comparison of computed flow rate (Simulation, full line) and PC-MRI measurements (MRI, dashed line) for the right IJV at C2/C3 level.

## 5.2 Intracranial venous pressure increase

Figure 6 shows the maximum pressure drop across the stenotic vein, throughout one cardiac cycle, as function of the variation of the CSA, which represents the variation of the severity of the left IJV stenosis; results are shown for all three configurations of the confluence of sinuses considered. Computed pressure drop is in agreement with results reported in [42], with pressure drops larger than 1.3 mmHg for a CSA reduction higher than 50%, and with maximum values of about 2.5 mmHg. We note that in a normal subject the reported pressure drop is about 1 mmHg.

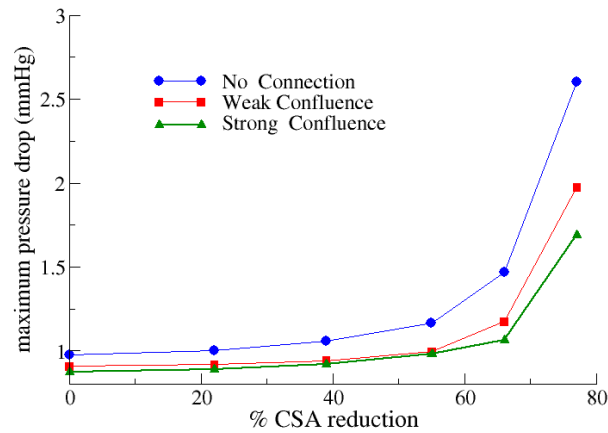


Figure 6: Maximum pressure drop (mmHg) across the stenotic IJV versus the reduction (in %) of CSA.

However, the result is highly depending on the morphology of cerebral veins. We remark that strongly connected left and right transverse sinuses have regulatory effects, allowing a redistribution of flow between the two IJVs. This aspect is further evidenced in Figure 7 (right). While flow is deviated from the left to the right IJV, pressure drop decreases in the stenotic left IJV (LIJV) due to the collateral path, and increases in the stenotic right IJV (RIJV), which is receiving more flow. For comparison, we simulated a pathological case where stenoses are present in both right and left IJVs (Figure 7, left), with CSA reductions of 77% (from 105 mm<sup>2</sup> to 24 mm<sup>2</sup>) and 50% (from 40 mm<sup>2</sup> to 20 mm<sup>2</sup>), respectively (Figure 7, left). The results are shown in Figure 7 (right). In this situation, the augmented resistance of the right IJV reduces the regulatory effect of the confluence of sinuses yielding a higher pressure also in the right IJV.

Finally, Figures 8 and 9 depict the computed pressures in the SSS and STS for the non-stenotic case, and for the case of stenoses in both IJVs. The maximum pressure increase in the SSS reaches 4 mmHg (from 9 mmHg to 13 mmHg) in the morphology without connection, while it remains relatively constant when transverse sinuses are connected. On the other hand, one can observe that a strong transverse sinuses connection, while reducing the pressure in the SSS, yields a pressure increases in the STS.

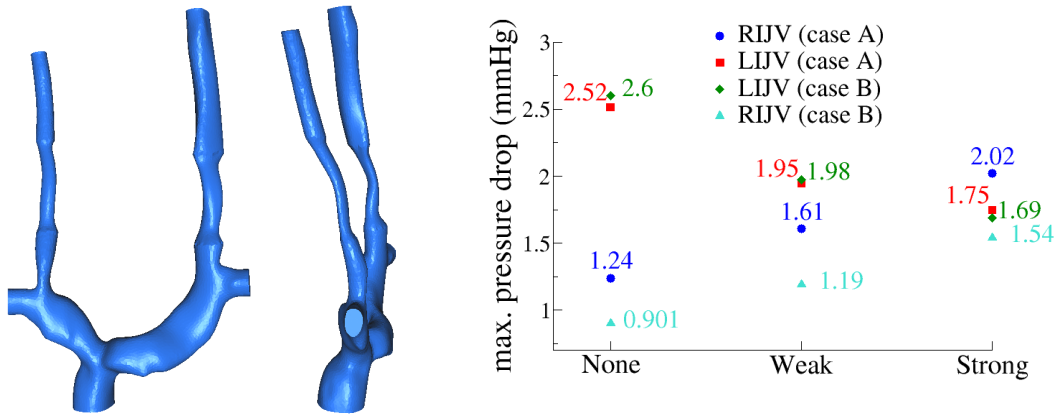


Figure 7: **Left:** Configuration with stenoses in both IJVs (frontal and lateral views). CSA reduction: 50% (right IJV) and 77% (left IJV). **Right:** Maximum pressure drop (for both left and right IJVs) depending on the degree of connection of confluence of sinuses, comparing the case of a single stenosis, case A (left IJV, CSA reduction of 77%) and stenoses in both IJVs, case B (CSA reduction of 50% – right IJV – and 77% – left IJV).

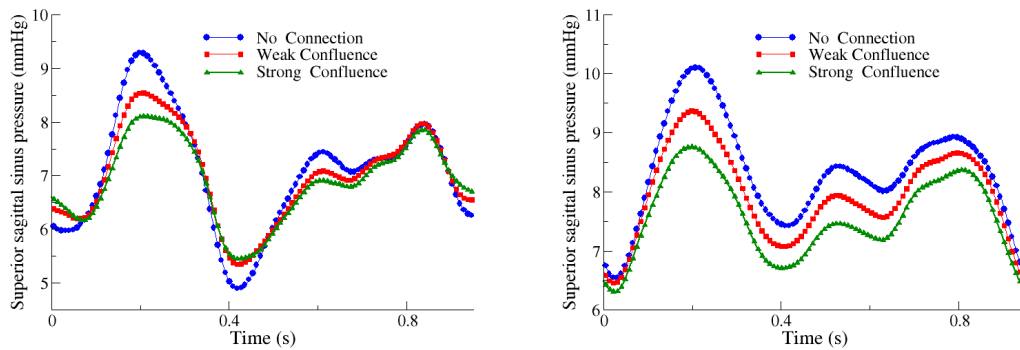


Figure 8: Computed pressure (in mmHg) in the SSS for different configurations of the confluence of sinuses. **Left:** Original geometry (no CSA reduction). **Right:** Left IJV CSA reduction of 77%.

### 5.3 Flow perturbation

The perturbation of the flow field (upstream and downstream) due to the stenosis is also a relevant aspect, which might have clinical implications. In Figure 10 (top) we show the peak velocity ratio, i.e. the ratio between pre-stenotic and post-stenotic velocity, for the different stenotic configuration and for the different considered topologies. In all cases, values are larger than 2.5 for CSA reduction higher than 60%. These values are in agreement with the results of [18], where a peak velocity ratio of 2.5 was used to characterise stenosis in the SVC. On the other hand, the behaviour is almost independent from the existence of sinuses connection. In fact the peak velocity ratio is not very sensitive to maximum pressure drop magnitude for

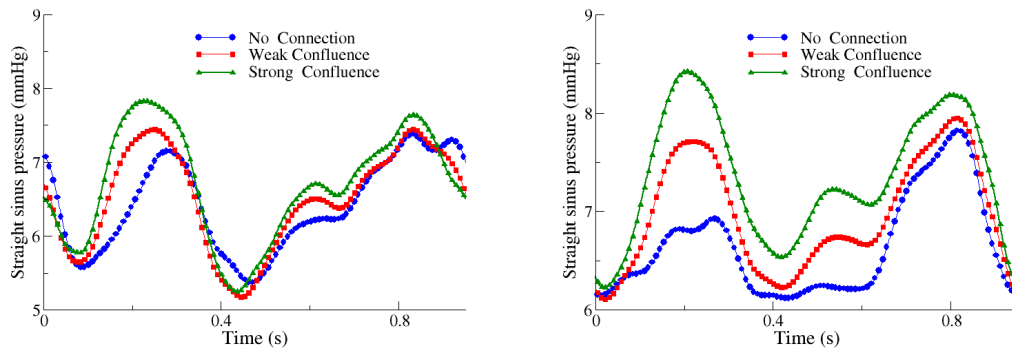


Figure 9: Computed pressure (in mmHg) in the STS for different configurations of the confluence of sinuses. **Left:** Original geometry (no CSA reduction). **Right:** Left IJV CSA reduction of 77%.

different configurations of dural sinuses, as we can see in Figure 10 (bottom).

Next, Figure 11 shows a snapshot of the streamlines near the stenotic region. One can clearly observe flow disturbances in the post-stenotic region, which, for severe stenosis degree, might lead to flow recirculation. A further quantity that might be perturbed by the presence of a stenosis is the WSS, depicted in Figures 12 to 14 for three selected points in space, located before, within and after the stenosis, respectively. While inside the stenotic area the WSS increases accordingly to the reduction of CSA (expected, as a consequence of higher peak velocity), one can observe an irregular behaviour when the occlusion reaches 50%, which results in a lower post-stenosis WSS.

The same effect can be observed from a different perspective in Figure 15, which shows the WSS over the surface of the 3D domain at time 0.2 s (corresponding to the maximum WSS in the non-stenotic configuration). Furthermore, Figure 16 depicts the surface OSI, an indicator of WSS perturbation, which quantifies the change in the periodic behaviour of shear stresses. Although the stenosis seems to have a moderate influence, due to the fact that the flow in the IJVs is mainly unidirectional, the area of highest perturbation is the one immediately after the stenosis and includes the brachiocephalic vein.

## 6 Discussion

### 6.1 Validation

Despite the several simplifications at the base of our computational model, we obtain a satisfactory agreement between computed IJV flow rates and patient-specific PC-MRI measurements (see Figure 5). The best match has been obtained for the left IJV flow rate for a *weak connection* of both transverse sinuses, which in this case corresponds to the patient morphology observed in the MRI images. It is worth noticing that this vein is the one where we focus our attention throughout this study. On the other hand, since many tributaries and collaterals that might contribute to cerebral venous flow are not taken into account in the present study,



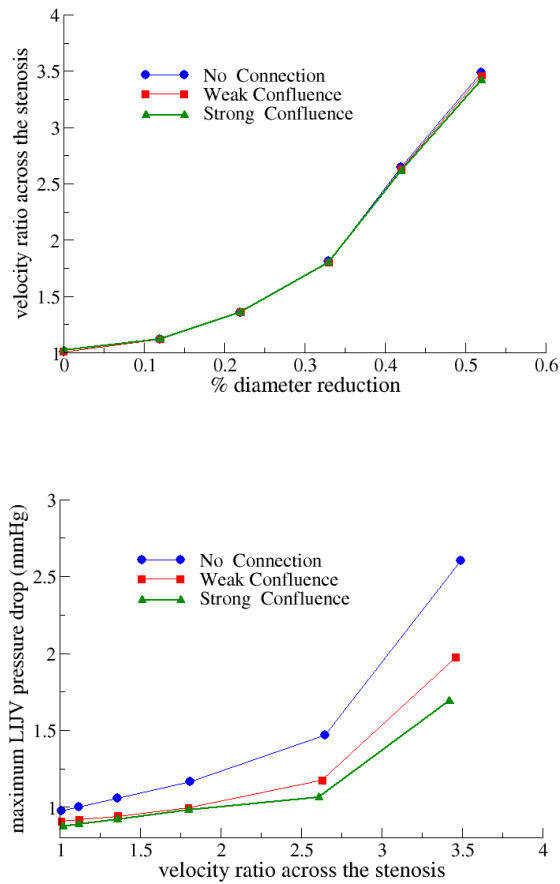


Figure 10: **Top:** Peak velocity ratio across the stenosis as function of relative reduction of its diameter. **Bottom:** Maximum pressure drop on LIJV as function of peak velocity ratio.

the model seems to underestimate flow in the right IJV. Moreover, as the following sections will show, we note that for stenotic IJVs our computational results are in agreement with reported values for pressure drop [42] and peak velocity ratio [18].

## 6.2 Pressure increase and importance of intracranial venous topology

The relation between CSA reduction and maximum pressure drop appears to behave exponentially when the CSA reduction is larger than 60% (Figure 6). This finding supports the indications given in a recent clinical study based on ultrasound imaging [18], in which only a CSA reduction higher than 75% was considered to be clinically significant.

On the other hand, we observe that the magnitude of the maximum pressure drop appears to be strongly correlated to the intracranial venous configuration. This is an aspect that, due to the technical complications in imaging minor veins, makes their investigation difficult, from an experimental point of view. The *no connection* configuration yields the most pronounced pres-

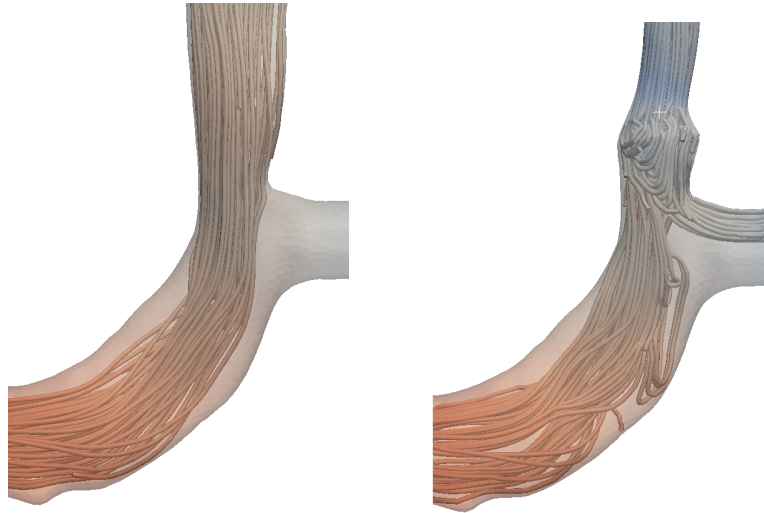


Figure 11: Snapshot of the streamlines near the stenotic area (time 0.2 s) for the simulation without confluence of transverse sinuses. **Left:** Non-stenotic configuration (CSA = 105 mm<sup>2</sup>). **Right:** Configuration with the largest occlusion (reduction of 77%, CSA = 35 mm<sup>2</sup>).

sure increase (Figure 6). For instance, a CSA reduction of 66% leads to a maximum pressure drops of 1.06, 1.17 and 1.47 (mmHg), for confluence of sinuses with *strong connection*, *weak connection* and *no connection*, respectively. This behaviour is, to some extent, to be expected, as in the *no connection* configuration the intracranial venous systems are separated circuits and the regulatory mechanism can not take place. However, it is interesting to see that a *weak connection* might already be able to bring the pressure to a normal value.

The effect of the morphology of the confluence of sinuses can also be seen in Figures 8 and 9. Comparing pressures in the SSS and STS, for non-stenotic and stenotic IJVs, we obtained higher dural sinuses pressures for the *no connection* case. For the non-stenotic case, peak pressures in SSS and STS are 9.3 vs 7.0 mmHg, for the *no connection* configuration and 8.0 vs 7.8 mmHg for the *strong connection* configuration. Similarly, for the stenotic case, pressures in SSS and STS are 11.0 vs 7.8 mmHg, for the *no connection* configuration and 8.7 vs 8.5 mmHg for the *strong connection* configuration. In the presence of well connected transverse sinuses, flow distribution can easily take place, yielding similar pressures in SSS and STS and lowering peak pressure values.

### 6.3 Flow field perturbation

The oscillatory behaviour of WSS, as well as abnormal WSS intensity have been reported as key factors influencing the morphology and disposition of endothelial cells [15]. There is medical evidence that pathological conditions are caused by low or highly oscillatory shear stress. In the context of our study, this potentially pathological condition can be observed in the post-stenotic area for all considered confluence of sinuses (see, *e.g.*, Figure 13). As expected, WSS inside the stenotic area is considerably higher than in pre- and post stenotic regions (Figures 12 to 14). As reported in [6], this higher shear stresses might induce morphological and histological changes in the affected IJVs. On the other hand, it is important to notice that

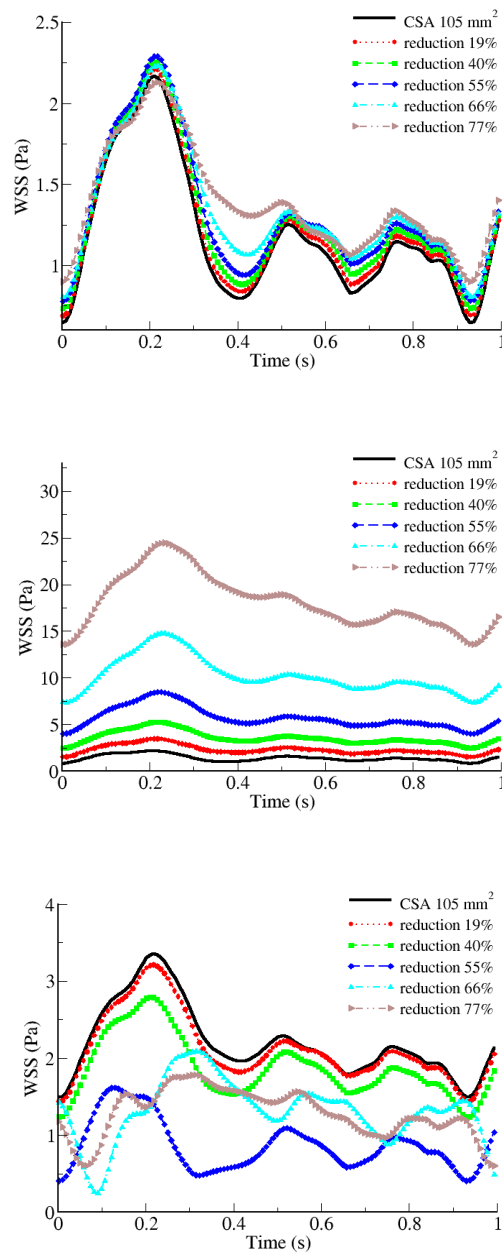


Figure 12: Behaviour in time of WSS at three selected points for the *no connection* confluence of sinuses configuration. **Top:** before; **Middle:** inside and **Bottom:** after the stenotic region.

the venous outflow in the IJV is mainly unidirectional, and reflux, which might take place for very short times in the case of strong CSA reduction (Figures 12 to 14) is limited to portions of the vessel after the stenosis.

We note that although WSS can also be computed using 1D models, these have serious limitations for producing physically meaningful results [16]. One limitation is to have to assume a velocity profile. The main motivation of the present work is to locally resolve the flow in 3

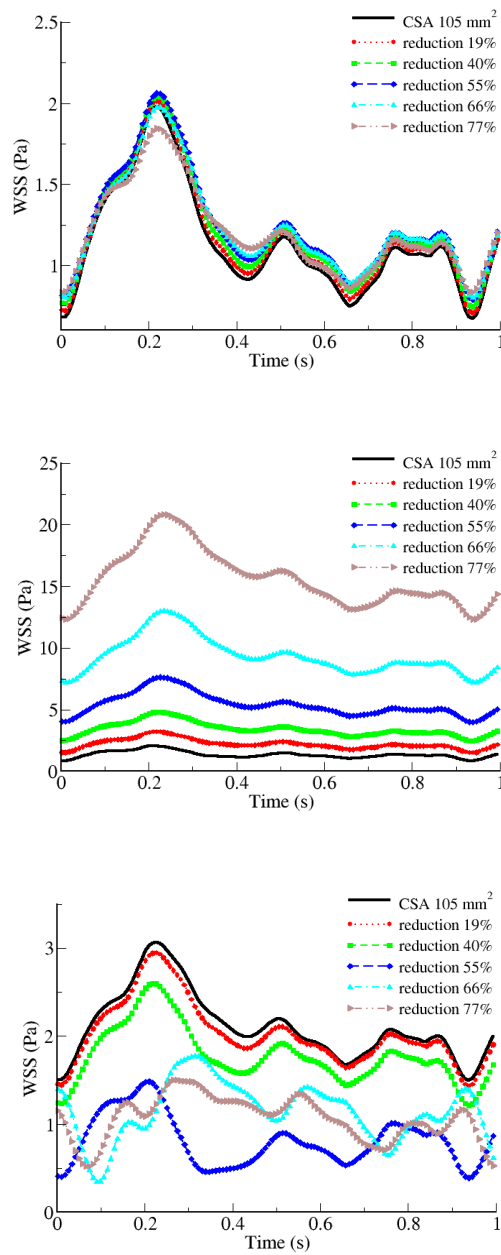


Figure 13: Behaviour in time of WSS at three selected points for the *weak connection* confluence of sinuses configuration. **Top**: before; **Middle**: inside and **Bottom**: after the stenotic region.

space dimensions so that computation of WSS and other physical quantities is physically more correct.

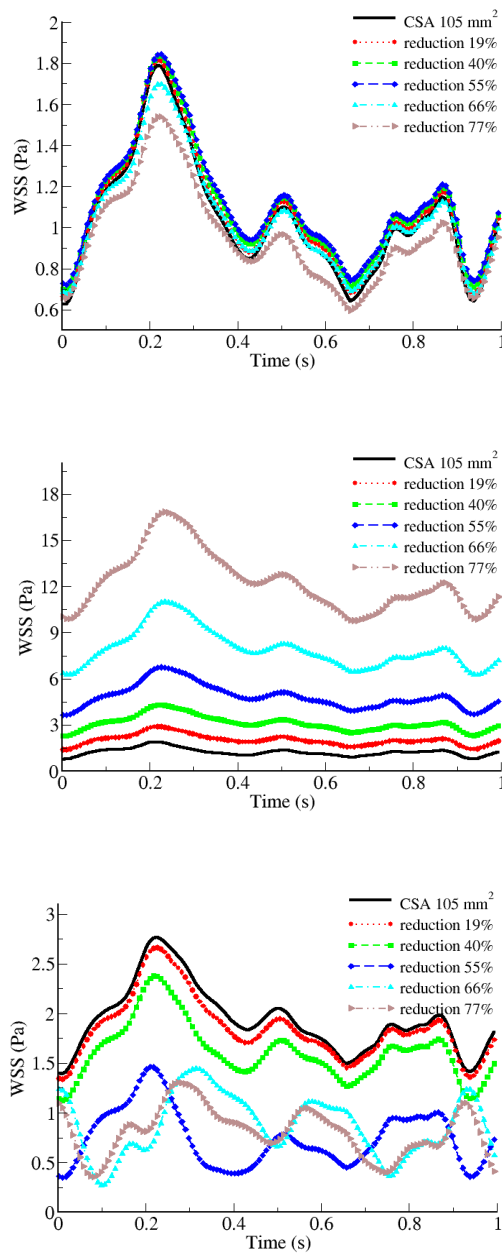


Figure 14: Behaviour in time of WSS at three selected points for the *strong connection* confluence of sinuses configuration. **Top**: before; **Middle**: inside and **Bottom**: after the stenotic region.

#### 6.4 Diagnosis criteria for IJV stenosis

Criteria for assessing the presence of a stenosis are currently defined according to the severity of the venous occlusion, i.e. based on the reduction of CSA below a fixed threshold [37, 42], or on the post- vs pre-stenotic peak velocities ratio [18]. Our computational results show that the peak velocity ratio criteria proposed in [18] is able to accurately identify a significant

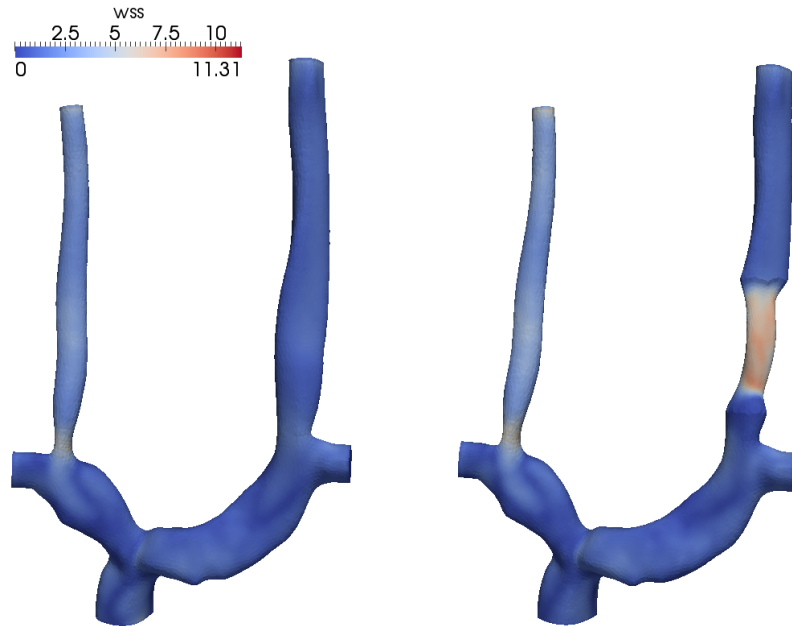


Figure 15: WSS magnitude on neck veins for the *strong confluence* configuration, at time  $t=0.2$ . **Left:** Non-stenotic configuration (CSA = 105 mm<sup>2</sup>). **Right:** Large occlusion (reduction of 66%, CSA = 35 mm<sup>2</sup>).

reduction of CSA, while it is not a relevant indicator for a pathological pressure drop, since peak velocity ratio for different intracranial venous configurations is almost identical (Figure 10), while pressure drops vary considerably (Figure 6). In the extreme cases considered, for a CSA reduction of 77%, peak velocity ratios for *no connection* and *strong connection* configurations are identical, while maximum pressure drops are 2.60 mmHg and 1.69 mmHg, respectively.

Another outcome of our study is that the criterion of a fixed threshold value of CSA, to identify clinically relevant stenoses, must be applied very carefully. For the particular configuration studied in this work, the right IJV would have been considered a stenotic vein, even in its physiological (sane) configuration. In fact, the impact of a stenosis in terms of pressure increase, which might yield pathological conditions in the cerebral venous system, is related not only to geometrical aspects (such as CSA reduction and, consequently high peak velocity ratio), but also to the flow rate across the stenosis. This aspect has been clearly shown for blood flow in different configurations of the confluence of sinuses (as discussed in Section 6.2). While CSA reduction and peak velocity ratio were identical for all intracranial venous morphologies, the related pressure increases differed considerably from case to case.

## 6.5 Model limitations

Although our model is based on patient-specific geometries and we achieve a satisfactory agreement with patient-measured flow data, some of the simplifications made in this study

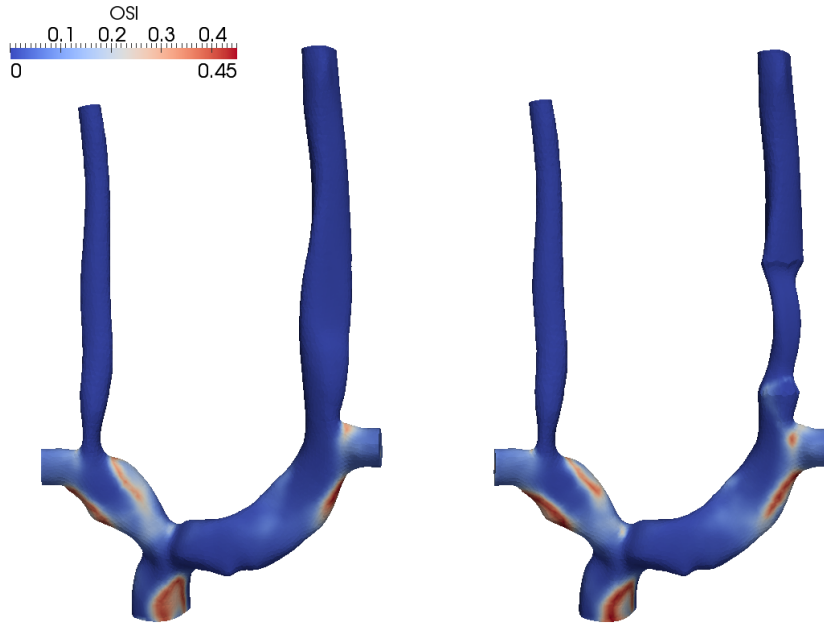


Figure 16: OSI near the stenosis for the case of sinuses without confluence. **Left:** Non-stenotic configuration (CSA = 105 mm<sup>2</sup>). **Right:** Configuration with the largest occlusion (reduction of 66%, CSA = 35 mm<sup>2</sup>).

must be underlined. In this study we have considered rigid vessel walls for the local 3D domain (IJVs). Although veins typically have a relatively high compliance, this simplification might be acceptable for a subject in supine position. In the case of a stenotic vessel, a compliant IJV would compensate a pressure increase by a volume change. In order to take this aspect into account, we introduced compliant intracranial vessels, modelled through a one-dimensional network, which allows to significantly reduce the computational complexity of the simulation. On the other hand, it is well known that these vessels are stiffer than neck veins, and, therefore, pressure changes must be considered as an upper-bound of a realistic situation. Another important aspect to be explored in future studies is the influence of alternative cerebral drainage pathways, such as vertebral veins, deep cervical veins, vertebral venous plexus and anastomoses between IJVs and external jugular veins. The presence of well developed collaterals might reduce the impact of a stenotic IJV on cerebral venous drainage.

## 7 Conclusions

We developed a computational framework to study, in a patient-specific setting, the effect of a stenosis of IJVs on cerebral haemodynamics. In particular, starting from individual images of the head and neck veins, and using patient-specific measured blood flow rates, we investigated the perturbation induced by stenoses of increasing severity in terms of *IJV and intracranial pressure increase and flow disturbances*, comparing the results against widely used clinical criteria for the diagnosis of stenosis. Furthermore, using a multi-scale mathe-

mational blood flow model we have been able to investigate *different topologies of intracranial veins*. Our computational study shows that currently used diagnosis criteria should be applied cautiously. In particular, a purely geometric criterion such as absolute CSA might be misleading, whilst a *local criterion*, such as the CSA ratio between pre- and stenotic portions of the veins (equivalent, to some extent, to a peak velocity ratio criterion) would be more significant. Moreover, we have illustrated the relevance of cerebral venous topology in relation to pressure increments caused by stenotic IJVs. This shows that well-connected transverse sinuses are much less sensitive to IJV stenoses than weakly connected ones. This suggests that the morphology of the cerebral venous system should also be taken into account as a relevant aspect, when diagnosing an IJV stenosis.

This work represents a first step towards a computer aided diagnosis of venous anomalies and venous insufficiencies, pathologies which are currently assessed only through criteria that do not consider patient specific anatomies. Further studies will extend the computational analysis taking into account anatomical data of a large set of individual geometries, in order to provide statistically significant trends. The property coupling of the local three-dimensional stenotic model to a closed-loop, global one-dimensional model will be the subject of future investigations.

## Acknowledgements

This work has been partially funded by CARITRO (Fondazione Cassa di Risparmio di Trento e Rovereto, Italy), project No. 2011.0214. The numerical simulations have been partially carried out with the finite element solver Mistral, developed in cooperation with Dr. J. F. Gerbeau and the research team REO, INRIA Paris-Rocquencourt.

## References

- [1] Antiga, L., Steinman, D.A.: Robust and objective decomposition and mapping of bifurcating vessels. *IEEE Trans. Med. Imag.* **23**(6), 704–713 (2004)
- [2] Berger, S.A., Jou, L.D.: Flow in stenotic vessels. *Annual Review of Fluid Mechanics* **32**, 347–382 (2000)
- [3] Bertoglio, C., Caiazzo, A., Fernández, M.: Fractional-step schemes for the coupling of distributed and lumped models in hemodynamics. *SIAM J. Sci. Comp.* **35**(3), 551–575 (2013)
- [4] Blanco, P.J., Pivello, M.R., Urquiza, S.A., Feijóo, R.A.: On the potentialities of 3D-1D coupled models in hemodynamics simulations. *Journal of Biomechanics* **42**, 919–930 (2009)
- [5] Chorin, A.J.: Numerical solution of the navier-stokes equations. *Mathematics of Computation* **22**, 745–768 (1968)
- [6] Coen, M., Menegatti, E., Salvi, F., Mascoli, F., Zamboni, P., Gabbiani, G., Bochaton-Piallat, M.L.: Altered collagen expression in jugular veins in multiple sclerosis. *Cardiovascular Pathology* **22**(1), 33 – 38 (2013)



- [7] Correa, C.D., Hero, R., Ma, K.L.: A comparison of gradient estimation methods for volume rendering on unstructured meshes. *IEEE Transactions on Visualization and Computer Graphics* **17**(3), 305–319 (2011)
- [8] Dumbser, M., Eaux, C., Toro, E.F.: Finite volume schemes of very high order of accuracy for stiff hyperbolic balance laws. *Journal of Computational Physics* **227**, 3971–4001 (2008)
- [9] Dumbser, M., Toro, E.F.: A Simple Extension of the Osher Riemann Solver to Non-conservative Hyperbolic Systems. *Journal of Scientific Computing* **48**, 70–88 (2011)
- [10] Formaggia, L., Gerbeau, J.F., Nobile, F., Quarteroni, A.: On the coupling of 3D and 1D Navier-Stokes equations for flow problems in compliant vessels. *Comp. Meth. Appl. Mech. Engrg.* **191**(6-7), 561–582 (2001)
- [11] Formaggia, L., Gerbeau, J.F., Nobile, F., Quarteroni, A.: Numerical treatment of defective boundary conditions for the Navier-Stokes equations. *SIAM J. Numerical Analysis* **40**(1), 376–401 (2002)
- [12] Fukusumi, A., Okudera, T., Takahashi, S., Taoka, T., Sakamoto, M., Nakagawa, H., Takayama, K., Kichikawa, K., Iwasaki, S.: Anatomical Evaluation of the Dural Sinuses in the Region of the Torcular Herophili Using Three Dimensional CT Venography. *Academic Radiology* **17**, 1103–1111 (2010)
- [13] Guermond, J., Mineev, P., Shen, J.: An overview of projection methods for incompressible flows. *Comput. Methods Appl. Mech. Engrg.* **195**, 6011–6045 (2006)
- [14] Guibert, R., McLeod, K., Caiazzo, A., Mansi, T., Fernández, M., Sermesant, M., Pennec, X., Vignon-Clementel, I., Boudjemline, Y., Gerbeau, J.F.: Group-wise Construction of Reduced Models for Understanding and Characterization of Pulmonary Blood Flows from Medical Images . Submitted to *Medical Image Analysis* (2013)
- [15] Haond, C., Ribreau, C., Bouterin-Falson, O., Finet, M.: Laminar flow through a model of collapsed veins. morphometric response of endothelial vascular cells to a longitudinal shear stress non uniform cross-wise. *European Journal of Applied Physiology* **8**, 87–96f (1999)
- [16] Katritsis, D., Kaiktsis, L., Chaniotis, A., Pantos, J., Efstathopoulos, E., Marmarelis, V.: Wall shear stress: Theoretical considerations and methods of measurement. *Progress in Cardiovascular Diseases* **49**(5), 307–329 (2007)
- [17] Koo, B.K., Erglis, A., Doh, J.H., Daniels, D.V., Jegere, S., Kim, H.S., Dunning, A., De-France, T., Lansky, A., Leipsic, J., Min, J.K.: Diagnosis of ischemia-causing coronary stenoses by noninvasive fractional flow reserve computed from coronary computed tomographic angiograms. Results from the prospective multicenter DISCOVER-FLOW (Diagnosis of Ischemia-Causing Stenoses Obtained Via Noninvasive Fractional Flow Reserve) study. *J Am Coll Cardiol* **58**(19), 1989–1997 (2011)
- [18] Labropoulos, N., Pierce, M.B.K., Pappas, P.J.: Criteria for defining significant central vein stenosis with duplex ultrasound. *Journal of Vascular surgery* **46**(1), 101–107 (2007)

- [19] LaDisa, J.F., Dholakia, R.J., Figueroa, C.A., Vignon-Clementel, I.E., Chan, F.P., Samyn, M.M., Cava, J.R., Taylor, C.A., Feinstein, J.A.: Computational simulations demonstrate altered wall shear stress in aortic coarctation patients treated by resection with end-to-end anastomosis. *Congenit Heart Dis* **6**(5), 432–43 (2011)
- [20] Liang, F., Takagi, S., Himeno, R.: Multi-scale modeling of the human cardiovascular system with applications to aortic valvular and arterial stenoses. *Med. Biol. Eng. Comput.* **47**, 743–755 (2009)
- [21] Montecinos, G.I., Castro, C.E., Dumbser, M., Toro, E.F.: Comparison of solvers for the generalized riemann problem for hyperbolic systems with source terms. *Journal of Computational Physics* **231**, 6472–6494 (2012)
- [22] Müller, L.O., Toro, E.F.: A global multi-scale mathematical model for the human circulation with emphasis on the venous system. *International Journal for Numerical Methods in Biomedical Engineering* (2013). Submitted
- [23] Müller, L.O., Toro, E.F.: Well-balanced high-order solver for blood flow in networks of vessels with variable properties. *International Journal for Numerical Methods in Biomedical Engineering* (2013). In Press
- [24] Munson, B.R., Young, D.F., Okiishi, T.H., Huebsch, B.W.: *Fundamentals of Fluid Mechanics*, 6Th Ed, SI Version. Wiley India Pvt. Ltd. (2009). ISBN: 0470262842
- [25] Papaioannous, T., Stefanadis, C.: Vascular wall shear stress: Basic principles and methods. *Hellenic J Cardiol* **46**, 9–15 (2005)
- [26] Passerini, T., De Luca, M., Formaggia, L., Quarteroni, A., Veneziani, A.: A 3D/1D geometrical multiscale model of cerebral vasculature. *J. Eng. Math.* **64**, 319–330 (2009)
- [27] Pedley, T.J., Brook, B.S., Seymour, R.S.: Blood pressure and flow rate in the giraffe jugular vein. *Phil. Trans. R. Soc. Lond. B* **351**, 855–866 (2004)
- [28] Quarteroni, A., Formaggia, L.: Mathematical modelling and numerical simulation of the cardiovascular system. *Handbook of Numerical Analysis* **12**, 31–127 (2004)
- [29] Seeley, B.D., Young, D.F.: Effect of geometry on pressure losses across models of arterial stenoses. *J. Biomech.* **9**, 439–448 (1976)
- [30] Si, H.: TetGen: A Quality Tetrahedral Mesh Generator and a 3D Delaunay Triangulator. Tech. Rep. 1762, WIAS, Berlin (2013)
- [31] Temam, R.: *The Navier-Stokes equations, theory and numerical analysis*. Amsterdam' New York-Oxford (1977)
- [32] Thomas, J.B., Antiga, L., Che, S., Milner, J.S., Steinman, D.A.H., Spence, J.D., Rutt, B.K., Steinman, D.A.: Variation in the carotid bifurcation geometry of young vs older adults: Implications for geometric risk of atherosclerosis. *Stroke* **36**(11), 2450–2456 (2005)
- [33] Toro, E.F.: *Riemann Solvers and Numerical Methods for Fluid Dynamics: A Practical Introduction*, third edn. Springer-Verlag (2009). ISBN 978-3-540-25202-3

- [34] Toro, E.F., Siviglia, A.: Flow in collapsible tubes with discontinuous mechanical properties: mathematical model and exact solutions. *Communications in Computational Physics* **13**(2), 361–385 (2013)
- [35] Toro, E. F. and Millington, R. and Nejad, L. A. M.: Towards very high order Godunov schemes. In: E.F. Toro (ed.) *Godunov Methods. Theory and Applications*, vol. 1, pp. 897–902. Kluwer/Plenum Academic Publishers, New York, Boston and London (2001). Conference in Honour of S K Godunov
- [36] Troianowski, G., Taylor, C.A., Feinstein, J.A., Vignon-Clementel, I.E.: Three-Dimensional Simulations in Glenn Patients: Clinically Based Boundary Conditions, Hemodynamic Results and Sensitivity to Input Data. *Journal of Biomechanical Engineering-Transactions of the Asme* **133**(11) (2011)
- [37] Utriainen, D., Feng, W., Elias, S., Latif, Z., Hubbard, D., Haacke, E.M.: Using magnetic resonance imaging as a means to study chronic cerebral spinal venous insufficiency in multiple sclerosis patients. *Tech. Vasc. Interventional Rad.* **15**, 101–112 (2012)
- [38] Vignon-Clementel, I., Figueroa, C., Jansen, K., Taylor, C.: Outflow boundary conditions for 3D simulations of non-periodic blood flow and pressure fields in deformable arteries. *Computer Methods in Biomechanics and Biomedical Engineering* (2010) **111**(3), 502–513 (2010)
- [39] Westerhof, N., Bosman, F., DeVries, C.J., Noordergraaf, A.: Analogue studies of the human systemic arterial tree. *J. Biomech.* **2**, 121–143 (1969)
- [40] Yeung, J.J., Kim, H.J., Abbruzzese, T.A., Vignon-Clementel, I.E., Draney-Blomme, M.T., Yeung, K.K., Perkash, I., Herfkens, R.J., Taylor, C.A., Dalman, R.L.: Aortoiliac hemodynamic and morphologic adaptation to chronic spinal cord injury. *J Vasc Surg* **44**(6), 1254–1265 (2006)
- [41] Zamboni, P., Galeotti, R.: The chronic cerebrospinal venous insufficiency syndrome. *Phlebology* **25**, 269–279 (2010)
- [42] Zamboni, P., Galeotti, R., Menegatti, E., Malagoni, A.M., Tacconi, G., Dall’Ara, S., Bartolomei, I., Salvi, F.: Chronic cerebrospinal venous insufficiency in patients with multiple sclerosis. *J Neurol Neurosurg Psychiatry* **80**, 392–399 (2009)
- [43] Zamboni, P., Menegatti, E., Bartolomei, I., Galeotti, R., Malagoni, A., Tacconi, G., Salvi, F.: Intracranial Venous Haemodynamics in Multiple Sclerosis. *Current Neurovascular Research* **4**, 252–258 (2007)